Numerical Study of Solid-Rocket Motor Ignition Overpressure Wave Including Infrared Radiation

Jean-Baptiste Dargaud,[*] Julien Troyes,[†] Jean-Michel Lamet,[‡] Lionel Tessé,[‡] and François Vuillot[§]
ONERA–The French Aerospace Lab, F-92322 Châtillon, France
and
Christophe Bailly[¶]
École Centrale de Lyon, 69134 Ecully Cedex, France

The ignition overpressure wave generated during the pressure build-up of a solid-rocket motor is numerically investigated in this study. Numerical simulations are compared to the LP10 experiments, consisting of the horizontal firing of a scaled-down model for the Ariane 5 P230 booster. The present work aims at the prediction of the main characteristics of the ignition overpressure in the far field and the assessment of afterburning influence on both its formation mechanisms and its alteration by the jet plume. Two three-dimensional large-eddy simulations are performed, one considering inert flow and one modeling the afterburning. Infrared images of the plume are also computed with a dedicated radiation transfer solver. An overall good agreement with the experimental results is reported on amplitude and duration. Nevertheless, the reactive case is found to provide better results on amplitude and directivity. The signature is also better reproduced on the microphones near the jet centerline, and the emitted infrared intensity is well captured. Computations indicate that the formation of the shock wave is obtained by coalescence of compression waves emitted by the accelerating jet at early times. For the reactive case, computations show an increased interaction between the jet and the overpressure wave.

Nomenclature

A	=	area, m^2
a	=	ellipse x-axis length, m
b	=	ellipse y-axis length, m
C_s	=	sth far-field microphone
c	=	speed of sound, $m \cdot s^{-1}$
D	=	diameter, m
e	=	eccentricity
h	=	infrared field height, m
I	=	acoustic intensity, W
k	=	absorption index
l	=	infrared field length, m
M	=	Mach number
m	=	alumina complex refraction index
n	=	refraction index
p	=	pressure, Pa
R	=	shock traveled distance, m
t	=	time, ms
u	=	velocity, $m \cdot s^{-1}$
x, y, z	=	Cartesian coordinates
α	=	far-field microphone angle, deg
γ	=	ratio of specific heats
Δp	=	shock amplitude, Pa
Δt	=	time step, s
Δx	=	maximal grid cell size, mm
δ	=	duration, s
λ	=	wavelength, m
ρ	=	density, $kg \cdot m^{-3}$

Subscripts

0	=	isotropic shock initial characteristics
atm	=	atmospheric conditions
bu	=	properties at rupture instant
em	=	properties at ignition overpressure emission instant
i	=	stagnation value
ini	=	simulation initial characteristics
int	=	shock tube intermediate properties
iop	=	ignition overpressure properties
ir	=	infrared properties
j	=	nozzle exit plane properties
le	=	ignition overpressure leading front arrival time
max	=	ignition overpressure pressure maximum
nl	=	ignition overpressure nonlinear propagation predicted time
prop	=	propellant properties
s	=	far-field sensor index
st	=	shock-tube properties
theo	=	ideal seal rupture characteristics at sensor location
tr	=	ignition overpressure trailing front arrival time

Superscript

*	=	nozzle throat properties

*Ph.D. Student.
†Research Scientist (Corresponding Author).
‡Research Scientist.
§Deputy Head. Senior Member AIAA.
¶Professor, Laboratoire de Mécanique des Fluides et d'Acoustique, Unités Mixtes de Recherche — Centre National de la Recherche Scientifique 5509, 36 Avenue Guy de Collongue; currently Institut Universitaire de France, Paris. Senior Member AIAA.

I. Introduction

S OLID-PROPELLANT rocket motors (SRMs) are commonly used in military and in aerospace applications. Such motors equip the European launchers Ariane 5 [1] and Vega [2] and were used for the Space Shuttle [3]. When an SRM ignites, strong transient pressure waves are generated and expelled out the nozzle [3]. When these motors ignite in a silo, the expelled pressure waves reflect from the silo floor and propagate up over the vehicle in a process called ignition overpressure (IOP). However, when these motors ignite on an open launch pad, two types of pressure waves are propagated over the vehicle and surrounding structures: 1) direct reflection from the

pad and ground, also typically called IOP, and 2) propagation from the open end of the exhaust trench, typically called the duct overpressure.

Historically, the first studies were performed for silo-launched or ducted missiles in the framework of military applications. Broadwell and Tsu [4] developed a one-dimensional model for predicting generation and propagation of transient pressure waves based on linearized Euler's equations forced by mass and momentum source terms, thus linking overpressure amplitude to the rate of pressure rise in the combustion chamber. Moreover, they demonstrated an amplifying effect on the magnitude of the IOP due to afterburning of the reducer-rich exhaust with the air in the silo. This semi-empirical approach unavoidably requires ad hoc input parameters but provides reasonable IOP estimate for missiles and launchers [5]. A review of the prediction methodologies applied to the Space Transportation System (STS) design can be found in Ryan et al. [6]. However, a transient overpressure wave of unexpected strength was observed during the first flight of the Space Shuttle (STS-1). Various studies were then undertaken in the 1980s to characterize the acoustic environment of scale models and to design wave-damping systems [7,8]. Water bags and water injection were successfully used since STS-2 by quenching afterburning and damping acoustic waves through thermal and kinetic effects. In all of these studies, parameter calibrations were used to estimate pressure amplitudes of full-scale launchers from small-scale experiments. A thorough analytical study of IOP was also proposed by Ikawa and Laspesa [9], but derivation of scaling laws is rather tricky in view of the complexity of the problem. A realistic analysis should indeed include the three-dimensional geometry of the pad, the reactive turbulent flows, the nonlinearity of the wave propagation, and the possible addition of water.

In parallel to experiments, numerical studies have broken through over the last few decades thanks to the increase in computational resources. Buell [10] performed a pioneering three-dimensional simulation by solving Euler's equations to describe the nonlinear propagation of a shock wave through a launch pad. Colombier and Pollet [11] followed a similar approach on a half-launch pad by using a two-step method to improve the ignition simulation. The relation between the overpressure and the time derivative of the chamber pressure is again shown, and the blast wave is found to be generated when the nozzle flow becomes supersonic. More recently, Salita et al. [12] studied IOP generated by a silo launcher using different levels of modeling, from an order of magnitude analysis and semi-empirical methods to axisymmetric eulerian computations. One of the main conclusions drawn by the authors is the importance of afterburning for determining the IOP amplitude. Three-dimensional simulations based on Euler's equations for a gas-phase reacting flow were performed by Pavish and Deese [13] on Delta II and III launchers on their pads to estimate unsteady loads and by Engblom et al. [14] for a nonreacting flow. Majamaki and Lee [15] used the unsteady Reynolds-averaged Navier–Stokes equations, written for a non-reacting flow and closed by a k-ω turbulence model on two configurations of Delta IV vehicles, with an overall good agreement between flight data and numerical results. Salita [16] also investigated the influence of the reactive constants for a three-reactions Arrhenius law scheme involving seven species through RANS (k-ω) simulations of the Minuteman IOP in a silo. For completeness, liftoff acoustic environment was also investigated using large-eddy simulation (LES) by Shimizu et al. [17] and by Tsutsumi et al. [18], and modeling of the damping effect of water sprays has been carried out by Canabal and Frendi [19].

However, it remains difficult to draw physical rules or general design requirements, given the variety of studied configurations. A more comprehensive understanding is desirable and will help to implement efficient wave-damping systems on new launch pads [20]. As already mentioned previously, numerous physical phenomena are involved in the generation and the propagation of IOP waves. Computation of this transient as simple shock waves by using Euler's equations provides a first approximation, but the prediction of the whole overpressure sequence requires taking into account the presence of the turbulent jet flow, afterburning, and water injection. This is quite challenging in terms of accuracy with respect to the state

of the art of LES [21]. The present numerical contribution regarding the Ariane 5 launcher is a part of this overall effort.

A 1/35 subscale SRM of the Ariane 5 booster P230 was fired horizontally at the Fauga-Mauzac ONERA Center (CFM) in a free-jet configuration, following the modus operandi detailed by Varnier et al. [22]. Internal pressure was recorded by a sensor located in the combustion chamber while pressure histories in the far-field were recorded on a microphone array. The complete firing sequence was also recorded by a high-speed camera and the infrared (IR) signature of a portion of the plume was recorded by a camcorder.

In the present numerical work, the ignition overpressure observed during this test-case is investigated through LES. Fluid flow is assumed to be composed of 13 gaseous species, including alumina droplets as an equivalent gas and intermediate species for describing afterburning through the use of a reduced kinetic scheme. Infrared intensity is postprocessed by a dedicated solver at the camera frequency from a three-dimensional control volume of the jet flow. To highlight the possible effect of afterburning on the IOP phenomenon, an additional computation that does not take into account afterburning is also reported. In Sec. II, the experimental setup [22] is briefly summarized for completeness. Section III deals with numerical procedures, including LES and infrared radiative computations. Results are presented in Sec. IV. Temporal pressure signals and infrared pictures are compared to measurements, and discrepancies are investigated. The interaction between the jet flow and the ignition overpressure is also highlighted by comparing inert and reacting flow simulations. Finally, conclusions are drawn in Sec. V.

II. Experimental Setup

The study focuses on the LP10 SRM ignition sequence. This SRM is a scaled-down motor of the P230 SRM booster equipping Ariane 5 launcher, fired at the CFM. The motor is fired horizontally in a free-jet configuration above a tar-covered ground at a height equal to about 14 times the nozzle exit diameter D_j. The instrumentation setup is composed of acoustical and visual recording devices.

A. Instrumentation Description

Figure 1 is a sketch of the top view of the experimental setup. A high-frequency piezo electric pressure transducer P_{rear} is located inside the combustion chamber, near the nozzle. The far-field transducers C_s are arranged in one arc, in a horizontal plane at nozzle center height. Its origin is located at the nozzle throat center, and its radius is $71 D_j$. The antenna covers angles from $\alpha_1 = 20$ deg to $\alpha_5 = 60$ deg on one side of the jet, where α_s is the angle of the microphone C_s. Finally, the high-speed camera is equipped with a 25 mm lens that records an area extending from the nozzle exit to $l = 1.44$ m downstream the jet centerline with a height $h = 0.77$ m at a 2000 Hz sampling frequency. Every image is composed of 120×60 pixels, corresponding to a spatial resolution of 12×12.83 mm. The camera records pictures in a restricted IR domain, which spans radiative wavelengths from 8 to 9.3 μm. This range has been selected after examining measurements from other firings. Details of the experimental setup can be found in Varnier et al. [22].
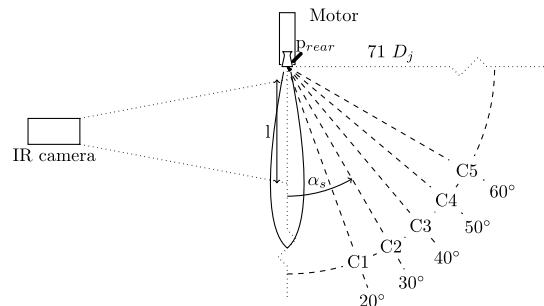

Fig. 1 Chamber pressure sensor position, far-field transducers location, and video setup.

B. Motor Properties

1. Motor Geometry and Propellant Disposition

The propellant is composed of 5% aluminum in mass and is organized in cylindrical and conical segments. The hot gases produced during the propellant combustion are ejected from the cylindrical combustion chamber through a submerged convergent–divergent conical nozzle. The latter is characterized by a ratio between the exit area and the throat area of $A_j/A^* = 7.5625$. The motor is initially closed with an aluminum seal designed to rupture under a 14 bar overpressure.

2. Flow Properties at Nozzle Exit

The design exit Mach number is found to be $M_j = 3.17$ from isentropic relations, with $\gamma_{\mathrm{prop}} = 1.236$. The chamber pressure history during the ignition sequence is shown in Fig. 2, from −5 to 30 ms. Seal rupture occurs at $t_{\mathrm{bu}} = -1.24$ ms and is followed by a pressure drop before a steep rise. The pressure build-up is 13.2 ms long, with a rise rate around 3.54 MPa $\cdot$ s^{-1}. Numerical simulations will start at time $t_{\mathrm{ini}} = 0$ ms, corresponding to the instant when pressure overcomes the seal rupture pressure.

The ratio of total to static pressure at the nozzle exit is $p_i/p_j = 60.14$. The ratio of the nozzle exit static pressure p_j to the atmospheric pressure p_{atm} is plotted on the right scale in Fig. 2; at early times in the ignition process, the jet is highly overexpanded and will present a series of compression shocks and expansion fans. As the pressure reaches its maximum, the jet becomes slightly underexpanded and will eventually again be overexpanded as pressure quickly goes down to its nominal value $p_{\mathrm{rear}} \approx 4.0$ MPa (not shown in the figure). Morrisette and Goldberg [23] found experimentally that the flow separation for the conical nozzle operating at a Mach number of 3.17 occurs when $p_j/p_{\mathrm{atm}} < 0.35$, as represented in Fig. 2 with a dashed line. Thus, no flow separation is expected to occur after the first 2 ms.

III. Numerical Procedure

Various experimental configurations were studied at CFM, from free jet to ducted firing with water quenching. They were used as a validation basis for developing a prediction methodology. In the first step, axisymmetric Navier–Stokes unsteady computations of free jets were performed by Troyes and Vuillot [24]. Computational domain did not include the combustion chamber. Indeed, taking into account the physics in the chamber requires modeling the propellant regression through the use of a particular boundary condition, which is not available in the code. These computations confirmed the strong influence of the afterburning and pressure rise rate on the overpressure amplitude and demonstrated a smaller influence of nozzle geometry. However, timing, amplitude, and directivity were not successfully reproduced, and this was blamed on the three-dimensional nature of the flowfield created by an axisymmetric nozzle flow bounded by a parallel flat ground plane. Further numerical studies were then carried out in a three-dimensional configuration [25], providing a better description of the experimental IOP in terms of amplitude and directivity. Consequently, in the
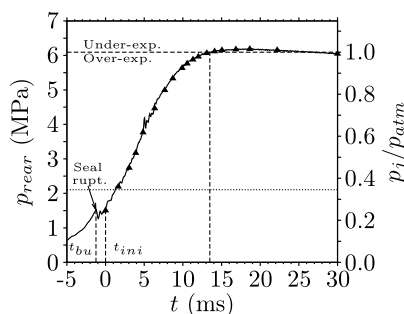
present study, large-eddy simulations using a Smagorinsky subgrid-scale model are carried out with the CEDRE software, a parallel multiphysics computational tool for numerical simulations in the field of energetics, with particular emphasis on propulsion applications, developed and validated at ONERA [26]. Gas-phase physics is governed by compressible Navier–Stokes equations [27]. IR intensity computation is carried out as a postprocessing with a Monte Carlo radiative solver [28]. Simulations focus on the start-up phase, ranging from t_{ini} to $t_{\mathrm{ini}} + 30$ ms (see Fig. 2).
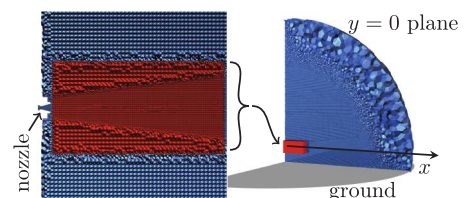
A. Computational Domain

The computational domain is built from a simplified geometry of the experimental setup. It includes the combustion chamber aft end, the nozzle, a part of the motor external structure, and the ground. The nozzle throat is the center of a hemisphere of radius $114D_j$ truncated by the ground in which the IOP propagates, as displayed in Fig. 3. It is split into two subparts, on which two solvers are activated independently. The radiative solver is used in a small cuboid of dimension $l \times h \times h$ (cf. Sec. II.A) that encloses the portion of plume visible by the IR camera, hereafter called the radiation domain, while the gas solver runs in both radiation and propagation domains.

B. Grid

The discrete geometrical model consists of a general polyhedral conforming mesh. A truncated cone that encloses the jet plume is defined in the grid-generation software. This refined zone extends from the nozzle exit to $73D_j$ downstream, with an aperture of 6.8 deg according to experimental measurements made by Koria and Lange [29]. The initial diameter is $2.57D_j$, and the final diameter is $20D_j$. The cell diameter inside this zone is set to $\Delta x = D_j/10$, yielding roughly 12.5 million cells. Outside this first region, the grid is generated to accurately capture the IOP wave propagation. The time scale of the IOP is taken as one-third of the wave front time duration δ_{iop}, which corresponds to the signal rise. From experimental time histories (see Sec. IV.B), $\delta_{\mathrm{iop}} \approx 3$ ms. The associated length scale is thus given by $\lambda_{\mathrm{iop}} = c_{\mathrm{atm}} \times \delta_{\mathrm{iop}}/3 = 0.346$ m. For a second-order space-discretization scheme, 20 points per wavelength are required to ensure low numerical dispersion and diffusion [30], which yields $\Delta x = 17.3$ mm. This criterion should be satisfied by the grid on the wave path between sources and microphones. Finally, the domain is stretched far from the zone of interest to provide a buffer zone that will damp the acoustic waves before they reach the boundary and hence prevent nonphysical wave reflection from the computational boundaries.

The grid is composed of generic polyhedral cells with various number of faces that can be assimilated to spheres of diameter Δx. With the criterion defined previously, the grid would contain more than 45 million extra cells, which unfortunately would not match the available computational power at time of calculation. Previous computations [31] have shown that prior attention should be brought upon jet discretization before propagation area refinement. The cell size is then scaled up outside the jet zone until the cell number is commensurate with the resources, yielding a final cell size $\Delta x = 30$ mm for 9 million cells. The main characteristics of the IOP are expected to be accurately described, but fine-scale structures will be damped by the numerical algorithm. Finally, 2 million more cells are required to mesh the nozzle and the transition region between the two main zones, yielding a total of 23.5 million polyhedral elements and 165 million faces.

Fig. 2   Time history of the combustion chamber pressure (left scale: combustion chamber pressure; right scale: nozzle exit static pressure over atmospheric pressure ratio; symbols: experimental points used as input for computations).

Fig. 3   Mesh view: details of the radiation domain and of the nozzle (left), and propagation domain in blue and infrared radiation domain inclusion in red (right).
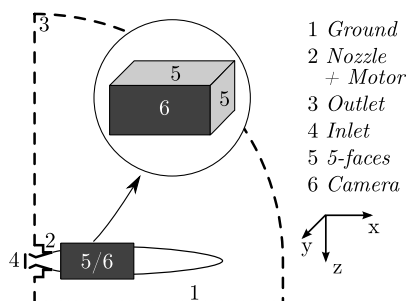
Fig. 4 Boundary schematic view and detail of the interface between radiation and propagation domains.

1 *Ground*
2 *Nozzle + Motor*
3 *Outlet*
4 *Inlet*
5 *5-faces*
6 *Camera*

C. Boundary Conditions

Figure 4 is a schematic view of the computational domain boundaries. The boundary condition applied for the ground (1) and the nozzle + motor case (2) grids is a no-slip adiabatic wall. The open-space limit outlet (3) is a nonreflective boundary at atmospheric conditions. Total pressure, total temperature, and uniform axial mass fraction injection of the considered chemical species are imposed on the inlet boundary (4). The total pressure history is specified as the measured time signal P_{rear} at arbitrarily chosen instants (see Fig. 2). Composition of the combustion products and flow total temperature are computed from experimental combustion chamber pressure and propellant composition, using an in-house thermodynamics equilibrium code.

Finally, the six faces of the interface between the two domains fall into two boundaries. The surface facing the camera ($+y$) on which radiative flux are computed is denoted camera (6), and the five other faces are named "5-faces" (5). They are both treated as interfaces in fluid mechanics computations. In the radiation computation, the boundary 5-faces is assumed to be a nonemitting black wall, while the limit camera is considered to be a black wall at an arbitrarily set temperature of 500 K (see Sec. III.E.2).

D. Flow Solver

Compressible Navier–Stokes equations are solved for the gas mixture [27]. A cell-centered finite-volume approach is applied. Interpolation follows a monotone upstream-centered scheme for conservation-law-type methodology, and numerical Euler fluxes are always upwind (Roe's flux difference splitting scheme) [32].

Time integration is obtained by a first-order Euler implicit method, with a global time step. Implicit linear system resolution is done by a generalized minimal residual method with block diagonal preconditioning. Parallelization of the flow solver is accomplished through a domain decomposition technique. Each core solves the equations on a small part of the whole domain, and the variables are exchanged from one part to another every time step. A different approach is followed for the parallelization of the radiation solver (see Sec. III.E.1). The time step Δt is set to 10^{-6} s, which yields a Courant–Friedrichs–Lewy number ($(|u| + c)\Delta t/\Delta x$ up to 10 in the highly stressed regions and still lower than unity in the regions where acoustics is a matter of concern.

Combustion products are composed of hot reducing species that may react with oxidizing ambient air when exiting the motor. Broadwell and Tsu [4], Troyes and Vuillot [24], and Salita [16,20] proved, with both theoretical and numerical studies, that the afterburning phenomenon has a strong influence on IOP amplitude. At this stage, no effort is made to reproduce the detailed chemical reactions, with the main point being the macroscopic effects on the IOP due to possible afterburning. A simple one-step eddy break-up model appears to be sufficient [33]. The choice of a more complex reduced kinetic scheme is dictated by the necessity to compute mass fractions of species required as input for the radiation computation. Three subsystems are considered [34]. A first set of equations characterizes the multistep chemistry of the H_2/O_2 system. A second set models the CO/CO_2 system, and the third assesses for the inhibitor effect of HCl. Reaction rates are computed from the classical Arrhenius law. A total of 12 species are involved in the system; seven are major species from motor exhaust gases or air (H_2, O_2, H_2O, HCl, CO, CO_2, and N_2), and five are intermediate species (H, O, OH, Cl, and Cl_2). Finally, inert alumina (Al_2O_3) is assumed to be in liquid state in the range of equilibrium temperatures considered (around 2300 K) and is added to the gaseous mixture. To avoid a very costly two-phase computation, an equivalent gas is substituted for the dispersed phase of alumina. Its thermodynamic properties are unknown a priori and are set so that the global thermodynamic properties of the mixture composed of the gaseous species and the equivalent gas are identical to the ones of the mixture composed of the gaseous species and the alumina droplets. All specific heat capacities C_p are given by seventh-order polynomial functions of temperature, except the alumina heat capacity, which is considered to be constant.

E. Radiation Solver

1. Presentation

The radiative transfer solver [28,35,36] is based on a Monte Carlo method. This approach consists of following a finite large number of energy bundles (discrete amounts of energy, which can be pictured as a group of photons bound together) throughout their transport histories, from emission to absorption. Bundle characteristics (namely wave number, initial direction, and emission point) and physical events (scattering, reflection off walls, except absorption) along bundle trajectories are chosen according to probability distributions by drawing random numbers. Absorption phenomenon is treated with the pathlength method [37], also called energy partitioning [38], which consists of computing exponential absorption along the path. Therefore, a bundle contributes to every cell it traverses. It is traced either until it leaves the computational domain or until its energy is depleted below a given cutoff level. Because all of the bundles are statistically independent, the solver parallelization is achieved by distributing them over the cores.

As well as the conventional forward method, different reciprocal methods, based on the exchange formulation of radiative transfer, are implemented: the emission, absorption, and optimized reciprocity methods [39,40]. In the case of the emission reciprocity method (ERM) [39], which has been carried out in the present work (see Sec. III.E.2), the radiative powers and radiative fluxes are calculated only in the cells and surface elements, respectively, which are source of energy bundles.

2. Adaptation

The solver has been initially developed to provide net radiative fluxes and powers integrated over the whole spectrum and all of the directions. For the present application, the solver has been restricted to reproduce the IR radiation in the experimental spectral range 8–9.3 μm only. Numerical IR images have been built by calculating radiative intensity from optical trajectories perpendicular to the camera boundary (see Fig. 4). To obtain this result, bundles have been emitted only from surface elements constituting the camera boundary. Every bundle initial direction has been systematically chosen perpendicular to this boundary, and their wavelengths have been selected in the filter spectral range. Then, the ERM has been applied along bundle trajectories to compute radiative intensity from jet flow. Note that, in this case, all of the trajectories contribute to the intensity received by the camera boundary. It would not be the case with the forward method or the other reciprocal methods. Indeed, due to scattering by alumina particles, all of the bundles emitted by the medium do not reach the receiving surface and do not contribute to the radiative intensity computation. The described method leads to the calculation of the intensity integrated over the considered spectral range in the direction perpendicular to the receiving surface, hereafter denoted as net intensity. Because the receiving surface is considered to be a black wall, the incident intensity is computed by adding the emitted intensity to the net intensity. The temperature of the receiving surface can then be chosen arbitrarily because it does not alter the incident intensity.

3. Exchange Between Solvers

In the present simulations, the gas solver informs the radiation solver with gas temperature, pressure, and species mass fractions every 0.5 ms. The volume fraction of alumina particles required for radiative properties computations is deduced from the alumina mass fraction and the density ratio of mixture (gaseous compounds and equivalent gas) to alumina.

4. Radiative Property Modeling

On the experimental spectral range, it has been assumed that only alumina particles, CO_2, and H_2O gaseous species in the radiation domain contribute to the intensity received by the camera boundary. Moreover, the absorption effect by the ambient air between the jet and the camera is neglected. A correlated-K model (CK) is used to compute absorption coefficients of CO_2 and H_2O gaseous species in the experimental spectral range. The CK model parameters used have been generated by Soufiani and Taine [41] for radiation in the infrared spectral range (1–67 μm) and for atmospheric applications in the 300–2500 K temperature range. For alumina droplets, particles are assumed to be spherical, homogeneous, and isothermal. Then, Mie theory is applied to calculate radiative properties, which are absorption and scattering coefficients and phase function. The alumina complex refraction index m is modeled as a function of wavelength λ_{ir} and temperature T in accordance with the expression given by Dombrovsky [42] such as

$$m = n(T, \lambda_{ir}) + ik(T, \lambda_{ir})$$

with the following expressions for the refraction index n and the absorption index k:

$$n(T, \lambda_{ir}) = \left[1 + \lambda_{ir}^2 \left(\frac{1.024}{\lambda_{ir}^2 - 0.003776} + \frac{1.058}{\lambda_{ir}^2 - 0.01225} + \frac{5.281}{\lambda_{ir}^2 - 321.4}\right)\right]^{0.5}$$

$$\times \left[1 + 0.0202\left(\frac{T}{1000} - 0.473\right)\right]$$

$$k(T, \lambda_{ir}) = 0.002(0.06\lambda_{ir}^2 + 0.7\lambda_{ir} + 1) \exp\left[1.847\left(\frac{T}{1000} - 2.95\right)\right]$$

where λ_{ir} is expressed in μm. Particles are considered to be at thermal equilibrium with the gases due to the equivalent gas approach used in the flow solver. Size distribution is approximated by a Gaussian function with a standard deviation equal to 10% around a mean diameter. Several values of the mean diameter have been tested. Results are presented in Sec. IV.D.

F. Initial Conditions

The whole domain including the nozzle is filled with air at atmospheric temperature and pressure. This is equivalent to the modeling of an ideal seal at the nozzle inlet. It differs from the experiment, where the seal is located shortly downstream of the throat and its rupture consumes energy through a mechanical effect. The difference in seal position is of the order of 50 mm and may induce a small time delay estimated at 0.15 ms for the seal break-up perturbation between experiments and numerical simulations.

G. Computation Conditions

For 30 ms of physical time simulated, the reactive fluid computation required 390 h elapsed on 1024 Harpertown cores, whereas the inert computation used a 480 Westmere cores cluster during 200 h elapsed. Each IR image postprocessing requires 5 min elapsed on 32 Nehalem cores.

IV. Results

A. Preliminary Observations

A time series of results taken from the inert computation is shown in Fig. 5. The three-dimensional surfaces of isopressure allow to visualize the IOP wave. A strong spherical front is already visible at $t = 0.5$ ms. It develops and reaches the ground at about $t = 3.5$ ms. The reflected wave can be observed in the subsequent images and crosses the jet plume at about $t = 7.5$ ms . This combination of the front and reflected waves propagates and is finally damped by the buffer zone at $t = 17.5$ ms. Note that the initial spherical wave takes
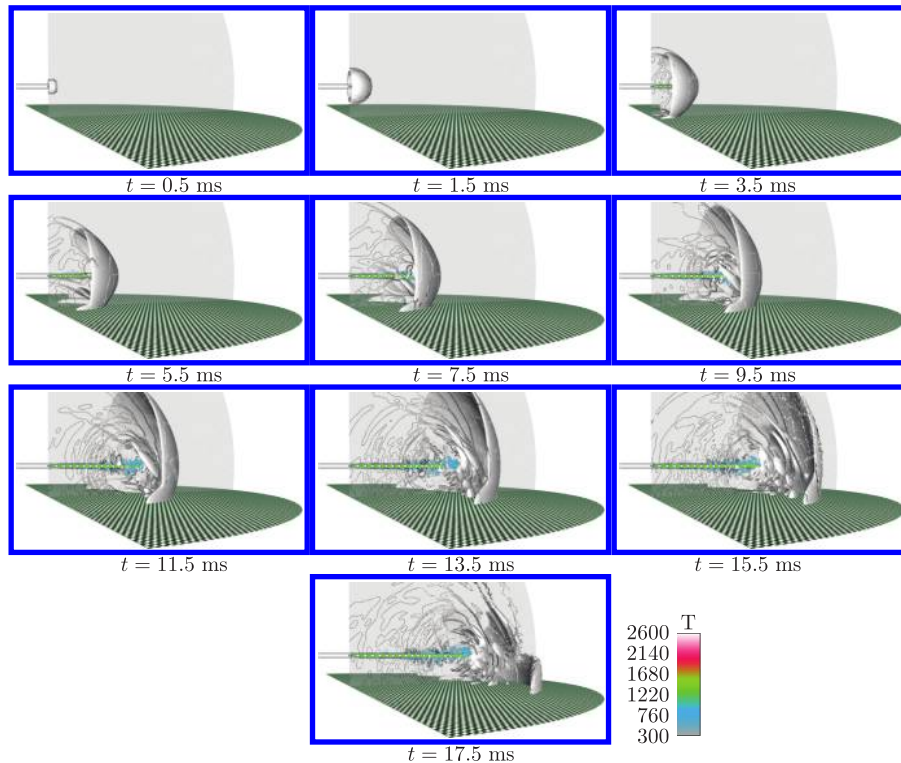
Fig. 5 Inert computation. Temperature maps, 5 pressure iso-contours from 101000 to 101600 Pa in $y = 0$ plane and 3D iso-surfaces of pressure at $p_{atm} + 500$ Pa.
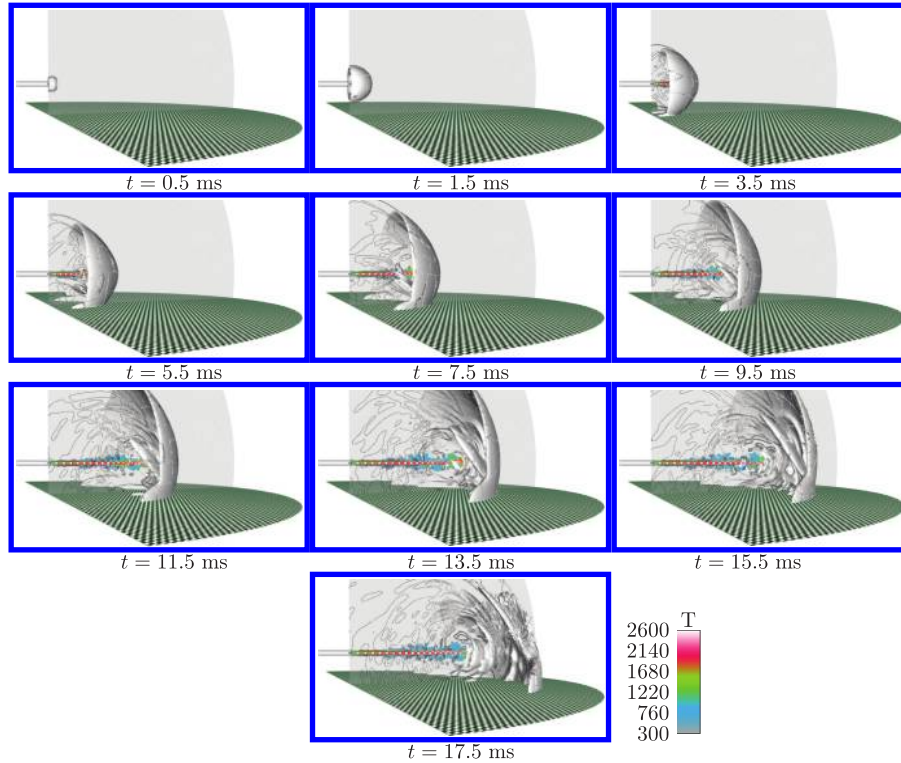
Fig. 6   Reactive computation. Temperature maps, 5 pressure iso-contours from 101000 to 101600 Pa in $y = 0$ plane and 3D iso-surfaces of pressure at $p_{atm} + 500$ Pa.

an ellipsoidal shape due to its convection by the jet flow. This change will be examined in Sec. IV.C. The jet development is monitored through the temperature map. Shock cells in the quasi-steady flow appears at $t = 3.5$ ms. At $t = 17.5$ ms, more than 15 cells are present.

A similar representation is displayed in Fig. 6 for the reactive simulation. Two major differences are noticeable. First, the inert computation predicts a jet velocity that is lower than the speed of the overpressure wave front at $t = 11.5$ ms. The opposite situation is found for the reactive case in Fig. 6. Second, a stronger and more complex overpressure wave is generated in the reactive case.

B.   Acoustic Results

In this section, differences induced by afterburning in the radiated pressure field are investigated.

1.   Global Results and Directivity

Pressure signals recorded in the far field by microphones C_1 to C_5 are plotted in Fig. 7. Only the low-frequency content of the signals can be computed in our simulations with respect to the mesh restrictions discussed in Sec. III.B. The peak IOP at 20 deg is around 3000 Pa (0.435 psi). The seal rupture shock can be identified on the experimental signal (solid line); indeed, a small shock front ahead of the IOP signature is visible at the same instant on all microphones, around $t = 13.2$ ms, with roughly the same amplitude. It is most clearly observed on the side microphones C_4 and C_5. No similar feature is found on the numerical signals. To investigate whether the first peak is part of the IOP front as believed or of a very strong seal rupture shock, a nonlinear model is considered in Sec. IV.B.2. Then, IOP is defined between its leading front arrival time t_{le} to the moment when pressure goes back to atmospheric pressure after the reflection peak t_{tr}, as pictured in Fig. 7b.

Both computations predict fairly well the peak amplitude, decay, and duration of the IOP. Details of the time signature are, however, not captured by the simulations. Although the first front received by the five microphones is almost identical in timing and amplitude for both computations, the rest of the signal presents large discrepancies. First of all, for microphones C_2 to C_5, the second pressure peak in the

inert computation is always weaker, and the depression is stronger. Second, the numerical time histories present a third positive peak on C_1 and C_2 that can be identified with the reflection of the IOP through a close study of the animations. It is ahead of time on C_1 but perfectly timed on C_2. The reactive simulation matches the amplitude of the reflection, while the inert computation well underestimates it. Finally, the signals for microphone C_1 are opposite in phase after the
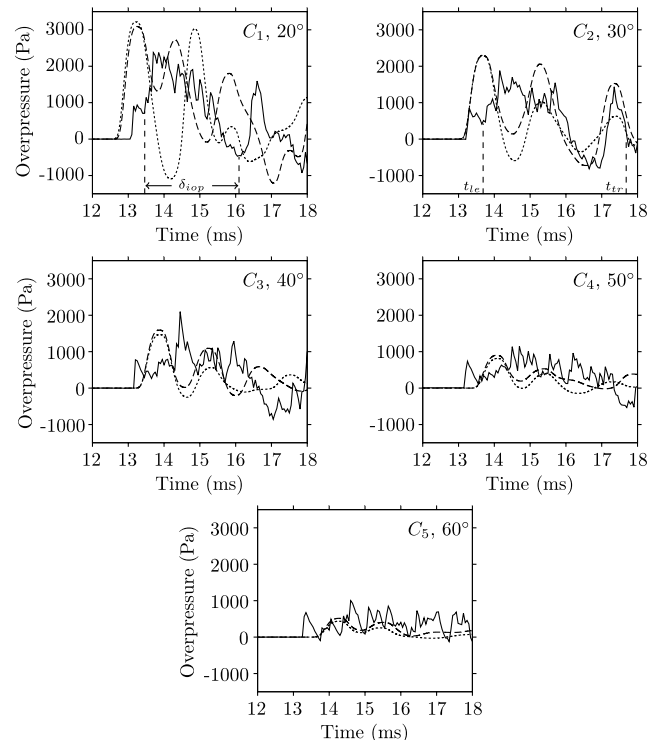
Fig. 7   Far-field time signals of pressure at the five locations C_1 to C_5 (refer to Fig. 1): experiment (—), reactive simulation (– –), and inert simulation (- - - - -).
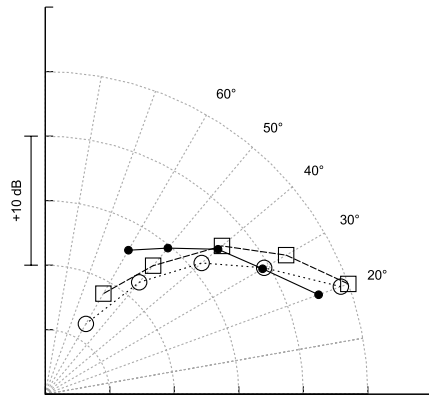
Fig. 8 Directivity of the IOP wave: experiment (—●—), reactive (—☐—) and inert simulation (- -⊝- -).
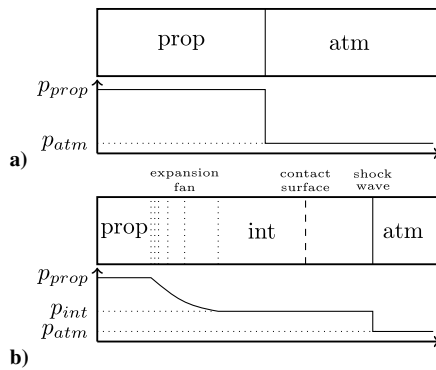
Fig. 9 Shock tube properties a) at initial state, and b) after diaphragm rupture.

first peak. The IOP in both computations presents two peaks. However, in the inert computation, a deep depression separates them, and the second peak arrives at a later time. This separation of the IOP is not explained for now, but afterburning has a an effect on the mechanisms responsible for the IOP shape. At this point, afterburning modeling seems to have two main effects: first, a strong alteration of the IOP near the jet axis, and second, an increase of the energy radiated in the sideline direction. The first point is studied in Sec. IV.C. The second point is highlighted by the directivity pattern represented in Fig. 8, where directivity is defined as the rms of pressure integrated over the IOP duration phenomenon $(t_{tr} - t_{le})$. Both computations overestimate the IOP by 2 dB on C_1, while the reactive one underestimates by 4 dB and the inert simulation by 7 dB on C_5.

2. Seal Rupture Shock

As seen in Fig. 7, no seal break-up shock is visible on the numerical signals. Then, one may try to identify the first front with a seal rupture shock of unusual strength, resulting from the ideal rupture (where no mechanical energy is consumed). To assess this assumption, the numerical and experimental shock amplitudes are compared to the magnitude of the shock resulting from an ideal seal rupture. It is modeled by a shock tube, where a diaphragm separates a pressurized chamber filled with hot propellant combustion products from a chamber filled with air at atmospheric conditions, as detailed in Fig. 9. As the diaphragm breaks, a shock forms and propagates in the low-pressure chamber to balance the pressure. Its amplitude $\Delta p_{st} = p_{int} - p_{atm}$ is computed from the Rankine–Hugoniot equations.

Also, for any perturbation under isotropic propagation, the conservation of acoustic intensity yields

$$\forall R > R_0, \qquad \Delta p = p - p_{atm} = \Delta p_0 \times R_0/R$$

where R is the traveled distance, and R_0 is the source volume characteristic radius of amplitude Δp_0. Here, R_0 is taken to be the

distance between the nozzle throat and the seal; $\Delta p_0 = \Delta p_{st}$ is the shock amplitude in the tube; and R is the distance between the nozzle throat and the microphones. This model yields the theoretical amplitude Δp_{theo} for an ideal seal rupture shock propagated from the seal to sensors. This value is found larger than the measured values recorded by all of the microphones C_s. IOP is a more powerful phenomenon than the seal break-up. If the first numerical fronts are actually part of the IOP, they are expected to be greater than the theoretical ideal seal break-up shock. The ratio between the numerical and the ideal overpressure amplitude is reported in Table 1. It is larger than unity only near the axis and lower than unity on the side microphones. This approach alone is not sufficient to draw conclusions regarding the first peak nature. Indeed, it has to be reminded that the computations do not model the seal as it stands in the experiment, but upstream of the nozzle throat. Going through the nozzle throat may have altered the computed seal break-up shocks and turned them into more directive shocks than experimental ones. The acoustic intensities of the shocks are then compared. On one hand, the considered shock acoustic intensity calculations are achieved by integrating the maximal pressure measured on the microphones on a spherical surface of radius $71D_j$ by assuming symmetry around the jet axis. For angles smaller than α_1, the pressure is taken constant and equal to the pressure measured on C_1. For angles between α_s and α_{s-1}, the pressure is taken to vary linearly between p_s and p_{s-1}. For angles greater than α_5, the corresponding amplitude is neglected. On the other hand, the ideal rupture shock acoustic intensity I_{theo} is deduced by integrating p_{theo} on the same surface.

Ratios of recorded to ideal shock-wave acoustic intensities are reported in Table 2. The experimental seal rupture shock has a much smaller acoustic intensity than the ideal seal rupture shock, while both computations have a higher intensity. This shows that the first peak captured in both computations results from a more energetic phenomenon than the seal rupture.

The absence of seal rupture shock in both computations is believed to be due to modeling issues, including the seal position as well as the chamber pressure rise rate reproduction. As seen in Fig. 2, computation origin of time is taken as the instant when pressure rises over seal break-up pressure, which occurs 1.05 ms after seal break-up. This delay duration is greater than the delay between the seal break-up shock and the IOP arrivals, as shown in Fig. 7, because the IOP propagates at a greater velocity than the seal break-up shock. No delay is introduced between the seal break-up and pressure build-up in simulations, and it is assumed that the seal rupture shock is overtaken by the IOP.

3. Ignition Overpressure Spatial and Temporal Origin

The computed first peaks are now identified to be part of the IOP phenomenon. On the experimental signals, the IOP is visible after the seal break-up shock. The delay between the rupture shock and the IOP arrival time is not constant with respect to the angle of measurement. Indeed, the IOP does not reach all of the microphones simultaneously. Two assumptions are formulated to explain this observation in what follows. First, differences in propagation duration can be attributed to nonlinear effects; and second, the IOP origin is not located at the array center, but downstream of the nozzle exit plane. Indeed, considering the amplitudes at stake, the propagation velocity is not constant along the path [43]. The relation

Table 1 First peak overpressure ratio

	Experiments	Inert LES	Reactive LES
$\Delta p_s/\Delta p_{theo}$	$\in [0.52:0.68]$	$\in [0.24:1.76]$	$\in [0.20:1.70]$

Table 2 Initial front acoustic intensity ratio

	Experiments	Inert LES	Reactive LES
I/I_{theo}	0.21	1.17	1.15

between the propagation velocity u of a shock of amplitude Δp is found from the Rankine-Hugoniot relations:

$$u^2 = c_{\text{atm}}^2 + \frac{\Delta p}{2\rho_{\text{atm}}}(\gamma_{\text{atm}} + 1)$$

The complete trajectory is then computed iteratively, from emission when $R = R_{\text{em}}$ and $\Delta p = \Delta p_{\text{em}}$ to the sensors, by assuming a constant velocity during a time step, yielding a nonlinear propagation duration δ_{nl}. IOP is defined at each microphone by its maximum pressure $\Delta p_{\text{max},s}$ and by the corresponding propagation duration $\delta_{\text{max},s}$. When assuming that the IOP is emitted at the nozzle exit, the estimated δ_{nl} for each set of measurements do not match the recorded $\Delta p_{\text{max},s}$; delays between two microphones are not comparable to the measured ones. Thus, for each set of measurements, the emission point is adjusted so that the difference of nonlinear propagation duration between two consecutive microphones is equal to the measured difference on the signal (i.e., $\delta_{\text{nl},s} - \delta_{\text{nl},s-1} = \delta_{\text{max},s} - \delta_{\text{max},s-1}$). This approach yields a location x_{em} downstream of the nozzle exit plane and an estimated propagation duration shorter than the effective one $\delta_{\text{max},s} - \delta_{\text{nl},s} = \text{constant} = t_{\text{em}}, \forall s > 2$ with t_{em} being the apparent IOP emission instant. Table 3 presents the results obtained for the three sets of data. The IOP origin in the reactive computation is found one diameter downstream the nozzle exit plane, at the same location as the experimental one, while inert computation predicts an origin one diameter further downstream. Both computations predict an IOP created sooner than the experimental one. This optimization was based on microphones C_2 to C_5 only. Indeed, $\Delta p_{\text{max},1}$ is always shorter than $\delta_{\text{nl},1}$. Moreover, at the creation instant (0.25 to 0.45 ms), no afterburning is expected, and then no difference in the generation of the IOP should be found. Then, this study should yield identical results for the two numerical waves, unless the propagation undergoes an alteration in every direction that cannot be accounted for by this simple approach, and that is different when afterburning is taken into account.

To confirm the spatial origin of the IOP, pressure and temperature time histories are recorded on a series of numerical sensors placed along the jet centerline from 0.75 to $2.25D_j$ after the nozzle exit plane every $0.3D_j$, as sketched at the top in Fig. 10. Pressure and temperature recorded on each of the six numerical sensors are drawn in Fig. 10. The temperature graph allows to track the contact surface (jet front) arrival time at each location. The pressure signal can be divided in two shock waves. First, a wave whose amplitude decreases with distance due to three-dimensional expansion and propagates at a constant speed in the environment at rest. It is identified as the seal rupture shock. This shock is followed by a second pressure rise. For sensors 1 and 2, this pressure rise coincides with the arrival of the jet, at $t = 0.25$ ms and $t = 0.28$ ms, respectively. However, the maximum of pressure for sensor 3 occurs when the jet front reaches sensor 2. For the next sensors, the pressure rises before the jet reaches the location. This indicates that compression waves are emitted by the accelerating jet and coalesce to form a strong shock wave, in a piston-like manner. This study confirms the trends deduced from the nonlinear propagation approach. A similar figure can be established for the inert computation, with similar pressure levels but a slightly lower jet temperature, and a slower jet. However, large discrepancies between the two computations are visible on the far-field signals, and the nonlinear approach predicted different behaviors. A modification of the IOP by the jet plume is to be expected and is certainly reinforced in the reactive computation. This will be assessed in the following paragraph.
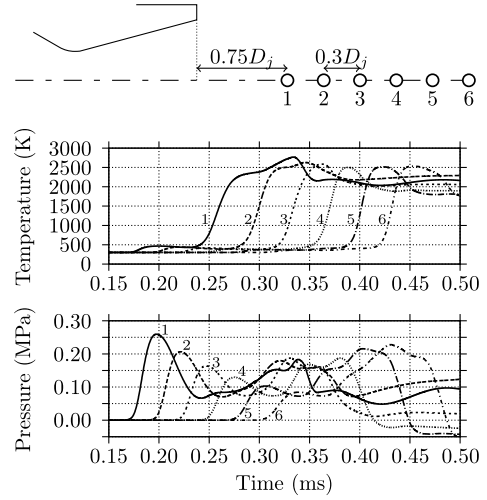
Fig. 10 Top: sketch of the numerical sensors located from 0.75 to $2.25D_j$ downstream of the nozzle exit. Middle and bottom: time evolution of the temperature and the overpressure for the reactive computation.
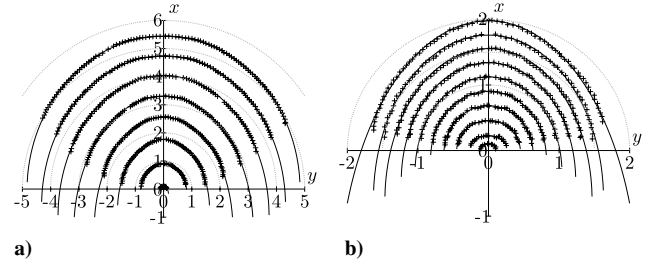
Fig. 11 Evolution of computed IOP front: extracted values from reactive computation (+); closest ellipse (—). a) $t = 0.5$ to 14.5 ms, every 2 ms; b) $t = 0$ to 5 ms, every 0.5 ms.

C. Jet Plume/Ignition Overpressure Interaction

Results from the previous subsection show that IOP is altered after its creation, hence during its propagation, and in greater extent when afterburning is taken into account. Also, a simple model study suggests that nonlinear effects occur in directions close to the jet axis. Observations from Sec. IV.A indicate that this might be due to the jet that interacts with the IOP. To assess this interaction, the isopressure line at $p_{\text{atm}} + 500$ Pa, which represents the IOP front, is extracted every 0.5 ms from the $z = 0$ plane and discretized. The elliptical shape of the IOP is highlighted by the circular grid drawn in thin lines in Fig. 11. Numerical points are then fitted with an ellipse:

$$\left(\frac{x - x_0}{a}\right)^2 + \left(\frac{y}{b}\right)^2 = 1$$
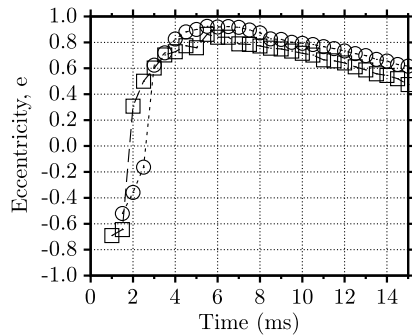
where a is the x half-axis, b is the y half-axis, and $(x_0, 0)$ is the ellipse center coordinates. Parameters a, b, and x_0 are evaluated for each new fit, and eccentricity e, which defines the ellipticity of the IOP front, is computed with the formula:

$$e = \text{sign}(a^2 - b^2)\sqrt{\frac{|a^2 - b^2|}{\max(a, b)^2}}$$

A small value characterizes a circular front, and a large value characterizes an elliptic front with the large axis oriented in the y direction in case of negative values and in the x axis for positive ones.

Eccentricity for both computations is plotted against time in Fig. 12. At early times, the large axis is in the transverse direction for both computations, with e presenting negative values. At $t = 2.5$ ms for the inert computation and 1.5 ms for the reactive one, the eccentricity changes its sign. From then, the large axis is in the x

Table 3   Propagation duration t_{em} and apparent emission location x_{em} obtained with the nonlinear approach

	Experiments	Inert LES	Reactive LES
t_{em}, ms	0.45	0.35	0.25
x_{em} (D_j)	1	2	1

Fig. 12 Eccentricity *e* against time: reactive simulation (—□—), and inert simulation (- -⊖- -).

direction. This change of shape is also visible in Figs. 5 and 6. Then, the IOP front eventually follows a less elliptic shape. The sudden change of sign is attributed to the plume jet/IOP interaction, and there is a significant difference between the two computations. To identify the reason for the discrepancies between the two computations, infrared radiation computations of the portion of interest of the jet are carried out.

D. Infrared Intensity

Radiation computations have been carried out with a total number of 48×10^6 bundles equally distributed over 32 cores, which ensures a good convergence of the calculation, with a standard deviation around 2–3%. Several droplet diameters have been tested, ranging from 1 to 10 μm, which are common sizes for solid-propellant rockets at operating conditions [44,45]. Incident IR intensity along the axial centerline on the camera boundary at $t = 3.5$ ms is extracted and plotted in Fig. 13 for each particle diameter for the reactive computation and with a 10 μm particle diameter for the inert case. The peaks of the curves correspond to the shock cells. Indeed, the gas temperature is increased when traversing a shock, and the flow at these locations consequently radiates more. Nine shock cells can be counted. All curves issued from the reactive computation are merged together, the intensity is then weakly dependent on particle diameter. Indeed, in the spectral range of interest, particle absorption coefficient does not vary a lot with diameter, while scattering is negligible compared to absorption. Therefore, given the weak dependence of the intensities on the particle diameter, the mean diameter has been arbitrarily set to 10 μm in the following computations.

Incident IR intensity fields at two key moments are displayed in Fig. 14. Only a qualitative comparison with experimental measurements is possible because the absolute scale is not available. The color scale is identical between the numerical figures and qualitatively comparable to the experimental one. At $t = 3.5$ ms, a large flare of hot gases is visible. This hot spot convected downstream the jet is well reproduced by the reactive computation; the length of the flare, whose the upstream point is identified in the figure with dashed lines, is comparable to the experimental one, even though the
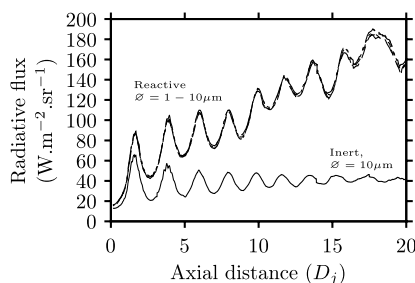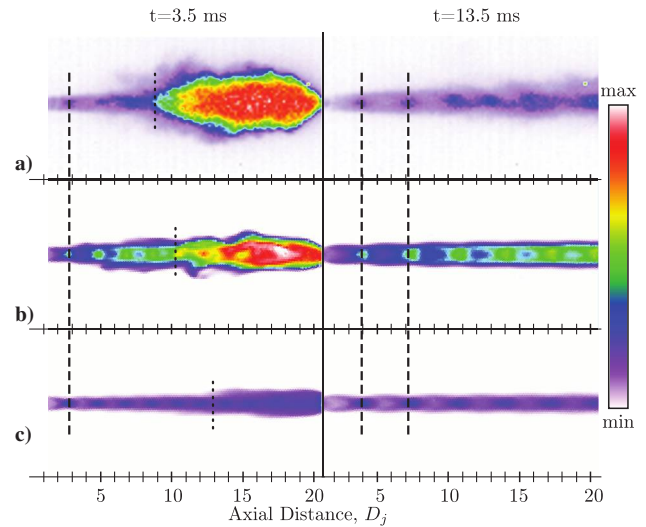
Fig. 14 Comparison between measured and computed incident IR intensities at $t = 3.5$ ms (left) and $t = 13.5$ ms (right): a) experiments, b) reactive computation, and c) inert computation.

computed flare is narrower. This flare is nearly nonexistent in the inert computation. It is highlighted in Fig. 13. Indeed, at the beginning, incident intensities are similar, but discrepancies rapidly increase after the first cell shock. The flare upstream extremity is located around the fourth cell, $\approx 10 D_j$, where a slope change is observed on the reactive computation incident intensity curves in Fig. 13. The difference reaches its maximum in the flare, where the incident IR intensity in the reactive computation is nearly five times higher than in the inert one.

Upstream of the flare, cell shocks are visible in both computations as well as on the experimental image at the same location, as indicated with the long dashed lines in Fig. 14. The nine cells in Fig. 13 are not discernible for the reactive computation due to the heat release from the afterburning but can be seen in the inert case. Later, at $t = 13.5$ ms, the shock cell structure of the jet is clearly visible. All images display six diamond-pattern shock cells, and the computations reproduce the location of the first cells accurately, as underlined by the dashed lines.

To ensure that the hot flare is actually caused by afterburning, the mass fraction of an intermediate species OH in the vertical median plane ($y = 0$) is displayed in Fig. 15 at the same moments as the ones selected for incident IR intensity fields in Fig. 14. Because OH is an intermediate species, its concentration depends essentially on its source terms due to its consumption and creation by the front flame. As such, it represents an excellent indicator of the flame location. The flare of high OH concentration visible at $t = 3.5$ ms corresponds to the hot flare on the incident IR intensity field. Later, afterburning occurs at the periphery of the jet and begins slightly downstream of the nozzle exit, due to ignition and mixing delays [44]. The afterburning flare then results from the sudden mixing of ambient air (oxidizer) and the propellant burnt products (reducers). It releases a large amount of heat and subsequently expands the gas and increases locally the speed of sound. The compression waves emitted ahead of the developing jet run faster in the reactive computation than in the inert one. The IOP is thus altered sooner, as shown in Fig. 12.

Fig. 13 Comparison between computed incident IR intensities for both simulations and different alumina particle diameters at $t = 3.5$ ms. Radiative flux is given in watts per square meter per steradian.
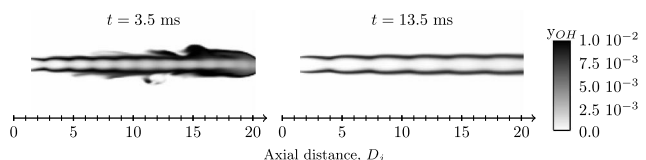

Fig. 15 OH mass fraction map in the vertical median plane $y = 0$ for the reactive computation.

V. Conclusions

The ignition overpressure observed during a small-scale solid-propellant rocket motor firing is numerically investigated in this paper. The ignition overpressure (IOP) far-field signal is reproduced, and a better understanding of the physical phenomenon responsible for IOP formation and propagation alteration is achieved. Afterburning during the start-up sequence is shown to be an important phenomenon to explain interactions between the jet plume and IOP.

The main features (amplitude and duration) of the IOP in the far field are well captured by the simulations. Discrepancies are, however, to be pointed out. First, neither computation reproduces the seal rupture shock. It is indeed quickly overtaken by the IOP in the computations due to modeling choices, including the seal position as well as a modification in the chamber pressure history. The initial pressure drop subsequent to the seal rupture is not applied in the computations. Second, the IOP directivity is overestimated in the downstream direction and underestimated in the sideline directions. This underestimation is most significant in the inert case, and reactive computation is then found relevant, especially for intermediate angles. In the inert computation, the second part of the IOP is of lower amplitude than the one in the reactive computation and may also be of opposite phase according to the considered microphone. Finally, IOP reflection on the ground is well reproduced and confirms the importance of taking into account the surroundings in the computation to achieve accurate predictions.

Furthermore, IOP is found to result from the coalescence of compression waves emitted by the early accelerating jet. This phenomenon occurs from one to two diameters downstream of the nozzle exit plane and begins roughly 0.35 ms after the computation starts. No difference between the two cases is visible at this point. The IOP shock wave is then altered by the jet plume at a later time, from 1 to 3.5 ms after computation beginning. Indeed, soon after exiting the nozzle, the jet mixes with ambient air to form a flare of hot gases, as captured by the experimental IR camera. This flare is very well reproduced by the IR radiation postprocessing in the reactive computation and is missing in the inert computation. The amount of heat released by this afterburning flare modifies the compression wave propagation speed emitted by the developing jet and thus modifies the way the jet acts upon the IOP. The present study could act as a guide for future work in numerical simulations of IOP in the near and far field.

References

[1] Chemoul, B., Louaas, E., Roux, P., Schmitt, D., and Pourcher, M., "Ariane 5 Flight Environments," *Acta Astronautica*, Vol. 48, Nos. 5–12, 2001, pp. 275–285.
doi:10.1016/S0094-5765(01)00026-1

[2] Bianchi, S., "VEGA, the European Small Launcher: Development Status, Future Perspectives, and Applications," *Acta Astronautica*, Vol. 63, Nos. 1–4, 2008, pp. 416–427.
doi:10.1016/j.actaastro.2007.12.058

[3] Ryan, R. S., Bullock, T., Holland, W. B., Kross, D. A., and Kiefling, L. A., "System Analysis Approach to Deriving Design Criteria (Loads) for Space Shuttle and Its Payloads. Vol. 1: General Statement of Approach," NASA TP-1949, 1981.

[4] Broadwell, J. E., and Tsu, C. N., "Transient Pressures Caused by Rocket Start and Shutdown in Ducted Launchers," *Journal of Spacecraft and Rockets*, Vol. 4, No. 10, 1967, pp. 1323–1328.
doi:10.2514/3.29079

[5] Simon, E. D., "Titan III Ignition Overpressure Attenuation," *19th AIAA/SAE/ASME Joint Propulsion Conference*, AIAA Paper 1983-1114, 1983.

[6] Ryan, R. S., Jones, J. H., Guest, S. H., Struck, H. G., Rheinfurth, M. H., and Verderaime, V. S., "Propulsion System Ignition Overpressure for the Space Shuttle," NASA TM-82458, 1982.

[7] Dougherty, N. S., and Mansfield, A. C., "6.4 Percent Scale Model SSV SRM/SSME Ignition Overpressure Verification Testing for Western Test-Range: Test Program at MSFC," NASA CR-171986, 1984.

[8] Counter, D. D., "Ignition Overpressure Study from Solid Rocket Motor Firings," NASA TM-86587, 1987.

[9] Ikawa, H., and Laspesa, F. S., "Ignition/Duct Overpressure Induced by Space Shuttle Solid Rocket Motor Ignition," *Journal of Spacecraft and Rockets*, Vol. 22, No. 4, 1985, pp. 481–488.
doi:10.2514/3.25776

[10] Buell, J. C., "Three-Dimensional Simulation of STS Ignition Overpressure," *17th AIAA Fluid Dynamics, Plasma Dynamics, and Lasers Conference*, AIAA Paper 1984-1629, 1984.

[11] Colombier, R., and Pollet, M., "Solid Rocket Motor Ignition Overpressure Prediction," *27th AIAA/SAE/ASME Joint Propulsion Conference*, AIAA Paper 1991-2437, 1991.

[12] Salita, M., Glatt, L., and Norton, C., "Modeling of Ignition Overpressure in Minuteman Silos," *33rd AIAA/ASME/SAE/ASEE Joint Propulsion Conference and Exhibit*, AIAA Paper 1997-2720, 1997.

[13] Pavish, D. L., and Deese, J. E., "CFD Analysis of Unsteady Ignition Overpressure Effect on Delta II and Delta III Launch Vehicles," *18th AIAA Applied Aerodynamics Meeting*, AIAA Paper 2000-3922, 2000.

[14] Engblom, W. A., Weaver, M. A., and Ndefo, E. D., "Numerical Study of Vehicle/Pad Configuration Effects on Launch Ignition Transients," *39th AIAA Aerospace Sciences Meeting and Exhibit*, AIAA Paper 2001-0802, 2001

[15] Majamaki, A. J., and Lee, J. W., "CFD Simulations of Launch Environments for Delta IV Vehicles at the SLC-6 Launch Pad," *49th AIAA Aerospace Sciences Meeting*, AIAA Paper 2011-1236, 2011.

[16] Salita, M., "Evaluation of CFD Code CFD-ACE for Rocket Applications," *36th AIAA/ASME/SAE/ASEE Joint Propulsion Conference and Exhibit*, AIAA Paper 2000-3186, 2000.

[17] Shimizu, T., Kodera, M., and Tsuboi, N., "Internal and External Flow of Rocket Nozzle," *Journal of the Earth Simulator*, Vol. 9, 2008, pp. 19–26.

[18] Tsutsumi, S., Fukuda, K., Takaki, R., Shima, E., Fujii, K., and Ui, K., "Numerical Study of Pressure Waves Generated by H-IIA Launch Vehicle at Lift-Off," *44th AIAA/ASME/SAE/ASEE Joint Propulsion Conference and Exhibit*, AIAA Paper 2008-5148, 2008.

[19] Canabal, F., and Frendi, A., "Study of the IOP Suppression Technique by Water Addition," *Journal of Space and Rockets*, Vol. 43, No. 4, 2006, pp. 853–865.
doi:10.2514/1.14861

[20] Salita, M., "Unanticipated Problems and Misunderstood Phenomena in and Around Solid Rockets," *47th AIAA/ASME/SAE/ASEE Joint Propulsion Conference and Exhibit*, AIAA Paper 2011-5956, 2011.

[21] Bogey, C., Marsden, O., and Bailly, C., "Influence of Initial Turbulence Level on the Flow and Sound Fields of a Subsonic Jet at a Diameter-Based Reynolds Number of 10^5," *Journal of Fluid Mechanics*, Vol 701, 2012, pp. 352–385.
doi:10.1017/jfm.2012.162

[22] Varnier, J., Prévot, P., Dunet, G., Barat, M., and Mazin, B., "Blast Wave and Afterburning at Ignition of Rocket Engines," *Proceedings of the 13th International Congress on Sound and Vibration*, International Inst. of Acoustic and Vibration, Vienna, 2006.

[23] Morrisette, E. L., and Goldberg, T. J., "Turbulent-Flow Separation Criteria for Overexpanded Supersonic Nozzles," NASA TP-1207, 1978.

[24] Troyes, J., and Vuillot, F., "Numerical Simulations of Model Solid Rocket Motor Ignition Overpressure Waves," *44th AIAA/ASME/SAE/ASEE Joint Propulsion Conference and Exhibit*, AIAA Paper 2008-5133, 2008.

[25] Troyes, J., Dargaud, J.-B., and Vuillot, F., "Numerical Simulation of Model Solid Rocket Motor Ignition Overpressure Waves. Part 2: Vertical Firing in Flame Duct," *Proceedings of the 17th International Conference on Sound and Vibration*, International Inst. of Acoustic and Vibration, Cairo, 2010.

[26] Scherrer, D., et al., "Recent CEDRE Applications," *ONERA Aerospace Lab Journal*, Vol. 2, 2011, http://www.aerospacelab-journal.org/al2 [retrieved June 2013].

[27] Refloch, A., Courbet, B., Murrone, A., Laurent, C., Troyes, J., Chaineray, G., Dargaud, J.-B., and Vuillot, F., "CEDRE Software," *ONERA Aerospace Lab Journal*, Vol. 2, 2011, http://www.aerospacelab-journal.org/CEDRE-Software [retrieved June 2013].

[28] Tessé, L., and Lamet, J.-M., "Radiative Transfer Modeling Developed at ONERA for Numerical Simulations of Reactive Flows," *ONERA Aerospace Lab Journal*, Vol. 2, 2011, http://www.aerospacelab-journal.org/Radiative-Transfer-Modeling-Developed [retrieved June 2013].

[29] Koria, S. C., and Lange, K. W., "An Experimental Study on the Behaviour of an Underexpanded Supersonic Gas Jet," *Archiv für das Eisenhüttenwesen*, Vol. 55, 1984, pp. 427–432.

[30] Bogey, C., and Bailly, C., "A Family of Low Dispersive and Low Dissipative Explicit Schemes for Flow and Noise Computations," *Journal of Computational Physics*, Vol. 19, No. 1, 2004, pp. 194–214. doi:10.1016/j.jcp.2003.09.003

[31] Dargaud, J.-B., Troyes, J., and Vuillot, F., "Numerical Simulation of Model Solid Rocket Motor Ignition Overpressure Waves. Part 1: Horizontal Free Jet with Reflective Ground," *Proceedings of the 17th International Conference on Sound and Vibration*, International Inst. of Acoustic and Vibration, Cairo, 2010.

[32] Courbet, B., Benoit, C., Couaillier, V., Haider, F., Le Pape, M. C., and Péron, S., "Space Discretization Methods," *ONERA Aerospace Lab Journal*, Vol. 2, 2011, http://www.aerospacelab-journal.org/Space-Discretization-Methods [retrieved June 2013].

[33] Troyes, J., Vuillot, F., Varnier, J., and Malbéqui, P., "Numerical Simulations of Rocket Solid Motor Engine Ignition and Duct Overpressure Waves at Reduced Scale," *45th AIAA/ASME/SAE/ASEE Joint Propulsion Conference and Exhibit*, AIAA Paper 2009-5133, 2009.

[34] Troyes, J., Dubois, I., Borie, V., and Boischot, A., "Multi-Phase Reactive Numerical Simulations of a Model Solid Rocket Motor Exhaust Jet," *42nd AIAA/ASME/SAE/ASEE Joint Propulsion Conference and Exhibit*, Paper 2006-4414, 2006.

[35] Tessé, L., Dupoirieux, F., and Taine, J., "Monte Carlo Modeling of Radiative Transfer in a Turbulent Sooty Flame," *International Journal of Heat and Mass Transfer*, Vol. 47, No. 3, 2004, pp. 555–572. doi:10.1016/j.ijheatmasstransfer.2003.06.003

[36] Tessé, L., Avila, S., Dupoirieux, F., and Taine, J., "Coupled Modeling of Aerothermochemistry: Soot Formation and Radiation in a Turbulent Diffusion Flame," *Proceedings of the 13th International Heat Transfer Conference*, Begell House Inc., Sydney, Australia, 2006.

[37] Farmer, J. T., and Howell, J. R., "Comparison of Monte Carlo Strategies for Radiative Transfer in Participating Media," *Advances in Heat Transfer*, Vol. 31, 1998, pp. 333–429. doi:10.1016/S0065-2717(08)70243-0

[38] Modest, M. F., *Radiative Heat Transfer*, 2nd ed., Academic Press, San Diego, CA, 2003, pp. 668–669.

[39] Tessé, L., Dupoirieux, F., Zamuner, B., and Taine, J., "Radiative Transfer in Real Gases Using Reciprocal and Forward Monte Carlo Methods and a Correlated-K Approach," *International Journal of Heat and Mass Transfer*, Vol. 45, No. 13, 2002, pp. 2797–2814. doi:10.1016/S0017-9310(02)00009-1

[40] Dupoirieux, F., Tessé, L., Avila, S., and Taine, J., "An Optimized Reciprocity Monte Carlo Method for the Calculation of Radiative Transfer in Media of Various Optical Thicknesses," *International Journal of Heat and Mass Transfer*, Vol. 49, Nos. 7–8, 2006, pp. 1310–1319. doi:10.1016/j.ijheatmasstransfer.2005.10.009

[41] Soufiani, A., and Taine, J., "High Temperature Gas Radiative Property Parameters of Statistical Narrow-Band Model for H_2O, CO_2 and CO, and Correlated-K Model for H_2O and CO_2," *International Journal of Heat and Mass Transfer*, Vol. 40, No. 4, 1997, pp. 987–991. doi:10.1016/0017-9310(96)00129-9

[42] Dombrovsky, L. A., "Possibility of Determining the Disperse Composition of a Two-Phase Flow from the Small-Angle Light Scattering," *High Temperature*, Vol. 20, No. 3, 1982, pp. 472–479.

[43] Morse, P. M., and Ingard, K. U., *Theoretical Acoustics*, McGraw–Hill, New York, 1968, Chap. 6.

[44] Simmons, F. S., *Rocket Exhaust Plume Phenomenology*, 1st ed., Aerospace Press, El Segundo, CA, 2000, Chaps. 2, 10.

[45] Sambamurthi, J. K., "Al_2O_3 Collection and Sizing from Solid Rocket Motor Plumes," *Journal of Propulsion and Power*, Vol. 12, No. 3, 1996, pp. 598–604. doi:10.2514/3.24075

J. Oefelein
Associate Editor